NANO · MICRO small
www.small-journal.com

Reduced Graphene Oxide Nanohybrid–Assembled Microneedles as Mini-Invasive Electrodes for Real-Time Transdermal Biosensing

Quanchang Jin, Hui-Jiuan Chen, Xiangling Li, Xinshuo Huang, Qianni Wu, Gen He, Tian Hang, Chengduan Yang, Zhen Jiang, Enlai Li, Aihua Zhang, Zhihong Lin, Fanmao Liu, and Xi Xie**

A variety of nanomaterial-based biosensors have been developed to sensitively detect biomolecules in vitro, yet limited success has been achieved in real-time sensing in vivo. The application of microneedles (MN) may offer a solution for painless and minimally-invasive transdermal biosensing. However, integration of nanostructural materials on microneedle surface as transdermal electrodes remains challenging in applications. Here, a transdermal H_2O_2 electrochemical biosensor based on MNs integrated with nanohybrid consisting of reduced graphene oxide and Pt nanoparticles (Pt/rGO) is developed. The Pt/rGO significantly improves the detection sensitivity of the MN electrode, while the MNs are utilized as a painless transdermal tool to access the in vivo environment. The Pt/rGO nanostructures are protected by a water-soluble polymer layer to avoid mechanical destruction during the MN skin insertion process. The polymer layer can readily be dissolved by the interstitial fluid and exposes the Pt/rGO on MNs for biosensing in vivo. The applications of the Pt/rGO-integrated MNs for in situ and real-time sensing of H_2O_2 in vivo are demonstrated both on pigskin and living mice. This work offers a unique real-time transdermal biosensing system, which is a promising tool for sensing in vivo with high sensitivity but in a minimally-invasive manner.

1. Introduction

Biosensors as simple handheld testing devices could provide rapid and early stage detection of human diseases or pathologies.[1–3] In particular, detection of hydrogen peroxide (H_2O_2), a signaling molecule in biological samples, plays a vital role in biosensing.[4–7] H_2O_2 (concentration varies from submicromolar to several hundreds of micromolar) is generally produced by many oxidases in mitochondria, regulating cellular growth and proliferation and involving in a wide range of biological processes.[8–10] Overproduction of H_2O_2 (>1×10^{-3} M) might associate with a variety of diseases such as cell damage that can even lead to senescence, neurodegeneration, and cancer.[11] Therefore, detection of H_2O_2 could offer direct indications of health states or disease progresses.[12–14] In addition, many biomolecules such as glucose or uric acid have been indirectly detected by applying specific enzymes to catalyze the generation of H_2O_2 by-products, which allows conversion of the H_2O_2 detection into the sensing of corresponding biomolecules.[8,15] A variety of advanced electrochemical biosensors based on nanomaterials, e.g., 2D nanomaterial graphene and reduced graphene oxide (rGO),[16–18] have emerged as promising bioelectronic and biosensor materials, due to their superior properties of charge transport, large surface area for interaction with a wide range of biomolecules, and good biocompatibility. A variety of hybrid nanocompositional materials employing graphene or rGO as matrix for immobilizing metal nanoparticles have also been fabricated as advanced electrochemical electrodes with enhanced sensitivity and responses.[19,20] For instance, graphene/Pt nanoparticle hybrid materials have been reported to construct ascorbic sensor,[21] dopamine sensor,[22,23] cholesterol biosensor,[24,25] and so on.[26,27] Most of the existing chip-based electrochemical biosensors were designed to detect target analysts in solution, which generally require transferring extracted biofluids such as blood, plasma, or urine onto the sensor chip and then performing sensing in vitro. This lacks the possibility of in situ and real-time sensing analysts in the in vivo environment. Real-time sensing analysts in vivo has been achieved by integrating biosensor onto a metal needle, which was employed to penetrate skin tissue or blood vessel to access the in vivo environment.[28–32] However, due to the invasive nature of needle penetration, this method tends to induce undesirable wounds and potential infection risks, limiting the possibility of long-term in situ sensing.

Q. Jin, Dr. H.-J. Chen, X. Li, X. Huang, Q. Wu, Dr. G. He, Dr. T. Hang, C. Yang, Z. Jiang, E. Li, A. Zhang, Z. Lin, Dr. F. Liu, Prof. X. Xie
The First Affiliated Hospital of Sun Yat-sen University
State Key Laboratory of Optoelectronic Materials and Technologies
School of Electronics and Information Technology
Guangdong Province Key Laboratory of Display Material and Technology
Sun Yat-sen University
510000 Guangzhou, China
E-mail: fanmao.liu@foxmail.com; xiexi27@mail.sysu.edu.cn

The ORCID identification number(s) for the author(s) of this article can be found under https://doi.org/10.1002/smll.201804298.

DOI: 10.1002/smll.201804298

Recently, microneedle arrays with each needle length of 500–800 μm have emerged as a convenient, painless, and mini-invasive transdermal technique, and have demonstrated great success in the fields of transdermal drug delivery.[33–37] For example, Xie et al. reported the applications of soluble microneedle to delivery peptide drugs for in situ therapy of neuropathic pain.[38] Besides transdermal drug delivery application, the applications of microneedles (MNs) as transdermal electrodes to continuous monitoring biomarkers have attracted increasing research interests.[15] For example, Hwa et al. have developed transdermal MN electrochemical sensor for continuous glucose detection;[39] Sharma et al. reported microneedle array as a continuous monitoring platform sensitive to glucose, lactate, and theophylline.[40] Barillaro and co-workers have developed a self-powered microneedle transdermal sensor for real-time measurement of glycemia in interstitial fluid.[21] However, the integration of nanostructural materials on MN surface as transdermal electrodes was rarely reported, while the existing MN-based electrodes are mostly based on monostructural material. This is largely due to the fact that nanostructures present on MN surface are likely to be mechanically destructed when MNs were inserted into skin tissue.

Here, we developed transdermal H_2O_2 electrochemical biosensor based on conductive microneedle patch, with Pt nanoparticles and reduced graphene oxide (rGO) nanostructural hybrid materials (Pt/rGO) present on MN surface (Pt/rGO MNs) as the active H_2O_2 sensing modulus (**Figure 1**a). The MNs were employed as a painless transdermal tool and as the carrier of

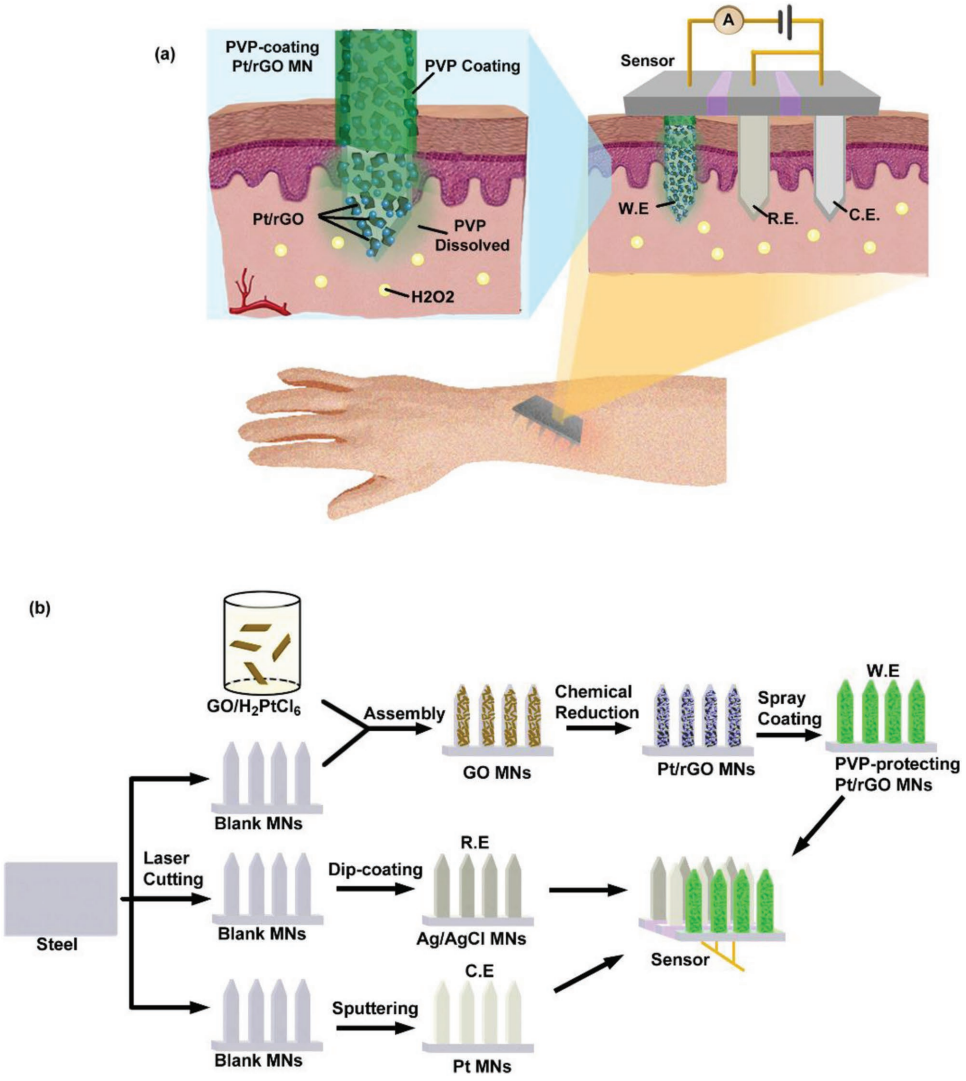

Figure 1. a) Illustration of the transdermal H_2O_2 electrochemical biosensor based on conductive microneedle patch with Pt/rGO present on MN surface as the active H_2O_2 sensing modulus. The MNs were employed to penetrate skin in a painless manner. The Pt/rGO nanostructures were protected from mechanical friction by a precoated PVP layer. The PVP layer was rapidly dissolved by the interstitial fluid after the MNs inserted into the skin. The Pt/rGO MNs were exposed for sensing H_2O_2 in vivo. b) Illustration of the fabrication procedure of the PVP-protecting Pt/rGO MN patch as a transdermal H_2O_2 electrochemical biosensor. The conductive MN patches were fabricated by laser micromachining, and nanostructural Pt/rGO were incorporated on the MN surface via LBL assembly followed by chemical reductions. PVP was spay-coated on the MNs to protect Pt/rGO. The Pt/rGO MN patch was used as the working electrode, and coupled with Pt MNs and Ag/AgCl MNs to be an electrochemical sensor.

bringing the Pt/rGO sensing modulus into the in vivo environment, while the Pt/rGO nanostructures were protected from the mechanical friction by a precoated water-soluble polymer layer. The polymer layer was readily dissolved by the interstitial fluid after the MNs inserted into the skin, exposing the Pt/rGO MNs for sensing H_2O_2 in vivo. The nanostructural Pt/rGO significantly improved the detection sensitivity of the MN electrode, and the sensing capability and sensitivity were preserved by polymer coating protection, free of destruction during MN insertion. The applications of the Pt/rGO MNs for in situ and real-time detection of H_2O_2 in vivo were successfully demonstrated both on pigskin and living mice. This work provided a unique real-time biosensing system, which could detect analysts in vivo with high sensitivity but in a mini-invasive manner.

The fabrication procedure of the Pt/rGO MN–based biosensor was illustrated in Figure 1b. Conductive metal MN patch was fabricated by laser microetching on a stainless steel substrate (thickness ≈ 100 µm, Section S1, Supporting Information). As shown in the scanning electron microscopy (SEM) image (**Figure 2**a1–a3), each MN length was designed to be 800 µm, which was sufficient to penetrate stratum corneum but not reached to the nerves or blood vessel in the dermis to induce pain. The width of each MN was 225 µm, with the inter-MN space of 250 µm, and totally ten needles in a patch. The MN was prepared with a sharp tip to facilitate skin penetration. Nanostructural Pt/rGO were prepared on MN surface via layer-by-layer (LBL) assembly method followed by chemical reduction. Aqueous solution containing 10 mg mL^{-1} graphene oxide (GO) and 0.5 mg mL^{-1} H_2PtCl_6 was sonicated for 2 h. The GO was dispersible in aqueous solution due to the existence of hydroxyl and carboxyl groups (Section S2.1, Supporting Information). The MN tips were repeatedly immersed into the as-prepared solution and then withdrawn and dried, allowing absorption of the solution onto the MN surface. As shown in the SEM images (Figure 2b1,b2), multiple layers of GO nanosheets were uniformly and conformally coated on the MN surface. After the coating, the MN surface exhibited nanostructural topography with slightly wrinkled morphology (Figure 2b3), corresponding to the GO nanosheet feature, yet the whole diameter of each MN was only increased by <10 µm (Sections S2.2 and S2.3, Supporting Information). The nonconductive GO on the MN surface was then reduced to be conductive rGO (Figure 2c) by immerging the MNs into aqueous solution of 10 mg mL^{-1} vitamin C solution at 95 °C for 3 h. At the same time, the vitamin C also reduced the H_2PtCl_6 to be Pt nanoparticles, which deposited on the rGO nanosheet surface. The rGO displayed more wrinkled morphology after chemical reduction, with nanoparticle dots with the size <50 nm homogenously distributed on the rGO surface (Figure 2d and Section S3.1 (Supporting Information)). The diameter of the individual MN was not significantly altered during the GO deposition and Pt/rGO

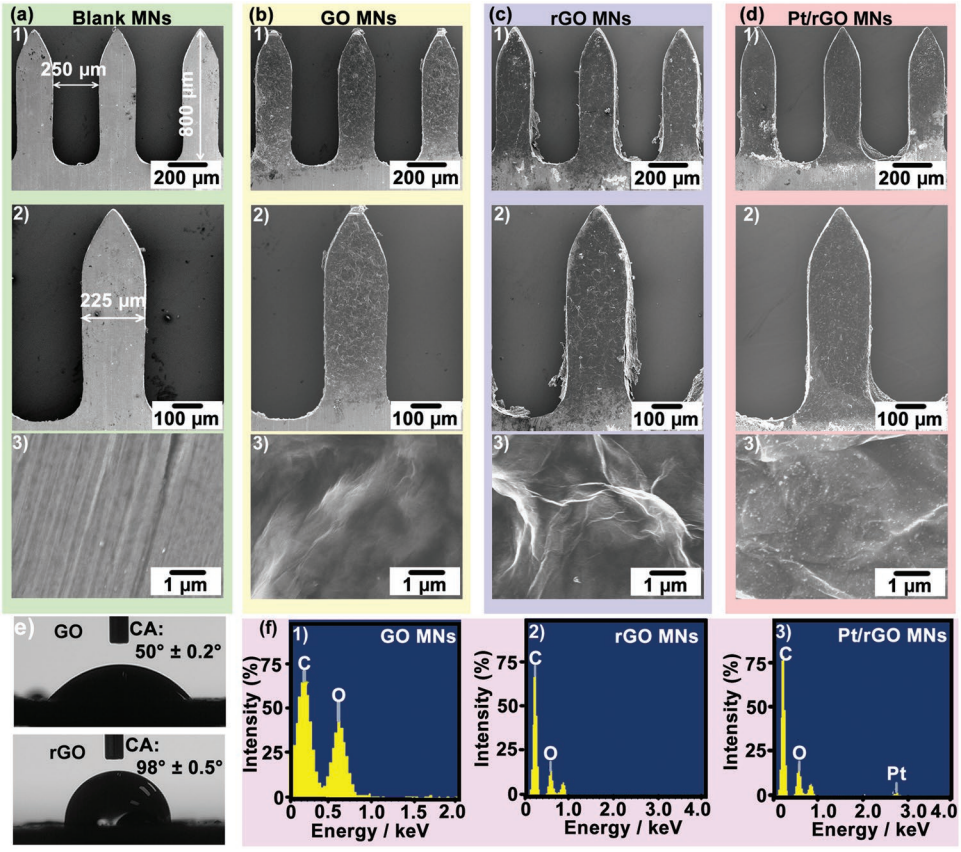

Figure 2. Characterization of Pt/rGO MNs. a–d) SEM images of the surface morphology of MN patch at different zoom-in magnifications. (a) Blank MNs, (b) GO MNs, (c) rGO MNs without Pt nanoparticles, and (d) Pt/rGO MNs. e) Water contact angle measurements on GO samples (up) and rGO samples (down). f) EDX spectrum of the surface of different MN patches, including 1) GO MNs, 2) rGO MNs, and 3) Pt/rGO MNs. The number ratio of C to O atoms contained in sample surfaces was analyzed.

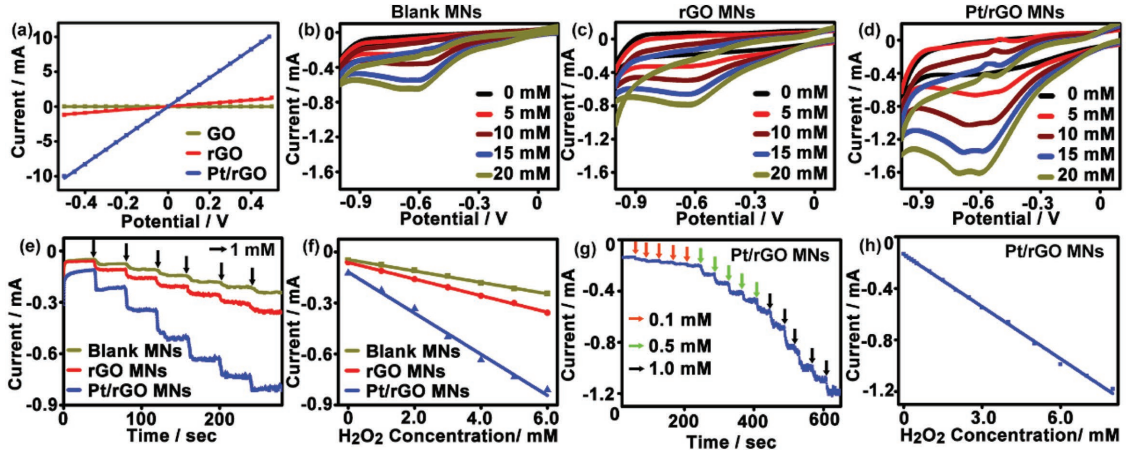

Figure 3. The in vitro electrochemical detection of H_2O_2 by using MN patch as working electrodes. a) The resistance measurements on Pt/rGO MNs, GO MNs, and rGO MNs. b–d) Cyclic voltammetry results of Blank MNs, rGO MNs, and Pt/rGO MN as working electrode upon sensing of H_2O_2 at different concentrations, at the potential range from −1.0 to 0.1 V. e) Amperometric responses of blank MN, rGO MN, and Pt/rGO MN electrodes upon the subsequent addition of H_2O_2 in PBS at the applied potential of −0.7 V. The H_2O_2 concentration was stepwise increased by 1×10^{-3} M every 40 s (black arrows), from 0 to 6×10^{-3} M. f) The relations of the steady-state currents in (e) and the corresponding H_2O_2 concentration. The data were linearly fitted. g) Amperometric responses of Pt/rGO MN electrodes upon the subsequent addition of H_2O_2 in PBS at −0.7 V. The H_2O_2 concentration was stepwise increased by 0.1×10^{-3}, 0.5×10^{-3}, and 1×10^{-3} M every 50 s (indicated with arrows). h) The relation of the steady-state current in (g) and the corresponding H_2O_2 concentration. The data were linearly fitted.

reduction processes. To confirm that the GO was successfully reduced to rGO, GO supported by a stainless steel substrate was treated with the same vitamin C reduction, and its contact angle to and its contact angle to deionized (DI) water was tested. The water contact angle significantly increased from 50° ± 0.2° to 98° ± 0.5° after reduction (Figure 2e), which was consistent with the fact that rGO tends to be hydrophobic due to the lack of hydrophilic groups (Section S2.1, Supporting Information). In addition, the elements of the MN surface were analyzed via energy dispersive X-ray spectroscopy (EDX) prior and after chemical reduction (Section S3.2, Supporting Information). Prior to reduction, the number ratio of C to O atoms in GO was closely 1:1 (Figure 2f1), while this ratio increased to 6:1 after reduction (Figure 2f2), suggesting that the GO was successfully reduced to rGO which contains less O atom ratio. Pt peak was detected as well, consistent with that Pt nanoparticles were generated forming Pt/rGO hybrid materials (Figure 2f3 and Section S3.2 (Supporting Information)). There are many oxygen-containing functional groups on GO surface, such as carboxyl, hydroxyl, and epoxide functional groups, performing as binding sites to anchor Pt ions. After oxygen reduction reaction, GO and Pt ions were turned into rGO and Pt nanoparticles. There were oxygen-containing functional groups and defects on rGO due to the incomplete reduction, which served as the anchoring sites for Pt nanoparticles and as chemically active sites for catalytic reactions.[41–43]

In our design, the oxygen-containing groups in GO nanosheets might provide large amounts of anchoring sites for the absorption of H_2PtCl_6, and facilitate the decoration of Pt nanoparticles on the rGO surface without aggregation after chemical reduction. Pt nanoparticles have been incorporated into many hybrid electrode materials due to their superior catalyzing capability of decomposing H_2O_2 to general electrochemical signals. The decorated nanosized Pt particles on the rGO sheet might render more accessible surfaces for the H_2O_2 electrocatalysis, and the rGO might offer fast charge transfer through the nanocompositions, contributing to higher electrochemical activity. To investigate the H_2O_2 sensing capability of the as-fabricated Pt/rGO MNs, the in vitro electrochemical detection of H_2O_2 at different concentrations was examined (Section S4, Supporting Information). The resistance of the Pt/rGO MNs was tested. MNs coated with GO prior to chemical reduction, and MNs with rGO coating only but without Pt nanoparticles were employed as control groups. The resistance of GO prior to reduction was in the range of 10^6 Ω, while the resistance of rGO after reduction was reduced to the range of 100 Ω. The decoration of rGO with Pt nanoparticles further reduced the resistance to the range of 10 Ω, about 10^5-fold lower than the MN prior to chemical reduction (**Figure 3**a). The electrochemical activities of the Pt/rGO MNs were evaluated via cyclic voltammetry (CV). Blank MNs without Pt/rGO coating, and MNs with rGO coating only were employed as control groups. The CV results of sensing H_2O_2 at the concentration of 0, 5×10^{-3}, 10×10^{-3}, 15×10^{-3}, and 20×10^{-3} M in phosphate-buffer saline (PBS) solution (pH 7.0) were shown in Figure 3b–d. No obvious reduction peaks were observed on blank MNs upon the addition of H_2O_2, except the increase of the background current (Figure 3b). The rGO MNs exhibited a slight reductive peak in the potential of −0.7 V in the presence of H_2O_2, which might be attributed to the reduction of carboxylic groups on rGO surface under the electrochemical condition (Figure 3c). By contrast, significant reductive peaks in the potential range of −1.0 to 0.1 V were observed on Pt/rGO MNs, attributed to the electrocatalytic effects of the Pt nanoparticles (Section S5.1, Supporting Information). The peak amplitude as well as the background current increased upon the increasing of H_2O_2 concentrations (Figure 3d). These results demonstrate the feasibility of quantitative detection of H_2O_2 in solution at the reductive potential of −0.7 V using the Pt/rGO MNs as working electrode.

The typical amperometric responses of blank MNs, rGO MNs, and Pt/rGO MNs upon H_2O_2 additions were tested at the

applied potential of –0.7 V. The H_2O_2 concentration was stepwise increased by 1×10^{-3} M every 40 s, from 0 to 6×10^{-3} M, which is within the typical H_2O_2 concentration (0.1×10^{-3}–10×10^{-3} M) in body.[8–11] The time points when H_2O_2 was increased were indicated with black arrows in Figure 3e. The electrical current immediately increased by ≈0.13 mA upon the addition of H_2O_2 concentrations and reached to a steady-state current. The addition of H_2O_2 solution induced higher current signal changes on the Pt/rGO MNs than those on the blank MNs or rGO MNs. The relations of the steady-state current and the corresponding H_2O_2 concentration were plotted in Figure 3f. The relations were almost in a linear manner in the range of 0–6×10^{-3} M H_2O_2 for all the three types of MN electrodes (Section S5.2, Supporting Information). The curve slope of the Pt/rGO MN sample was at least threefold higher than those of blank MNs and rGO MNs, indicating higher sensitivity of the Pt/rGO MN electrode. To demonstrate the Pt/rGO MN electrode could even detect lower concentration of H_2O_2 in solution, the typical amperometric response of the Pt/rGO MN electrode is to continuously detect various concentrations of H_2O_2 as low as 0.1×10^{-3} M (Figure 3g and Section S5.3 (Supporting Information)). The H_2O_2 concentration was stepwise increased by 0.1×10^{-3} M every 50 s up to 0.5×10^{-3} M, and then stepwise increased by 0.5×10^{-3} M every 50 s up to 3×10^{-3} M, and finally stepwise increased by 1×10^{-3} M every 50 s up to 8×10^{-3} M. The time points when H_2O_2 was increased were indicated with arrows in Figure 3g. The increasing concentration of 0.1×10^{-3} M could also induce detectable electrical signals of ≈0.01 mA. The relation of the steady-state current and the corresponding H_2O_2 concentration was shown in Figure 3h. The current signal increased with H_2O_2 concentration in a nearly linear relation, with the linear region extending to as low as 0.1×10^{-3} M (Section S5.3, Supporting Information). These in vitro sensing results successfully demonstrated that the functionalization of MNs with nanostructural Pt/rGO significantly improved the H_2O_2 sensing performance, and that the Pt/rGO MN electrode could detect H_2O_2 in solution with reasonable sensitivity and response (Sections S5.4–S5.6, Supporting Information).

The nanostructural Pt/rGO present on the MN surface (**Figure 4**a) played an important role on enhancing the

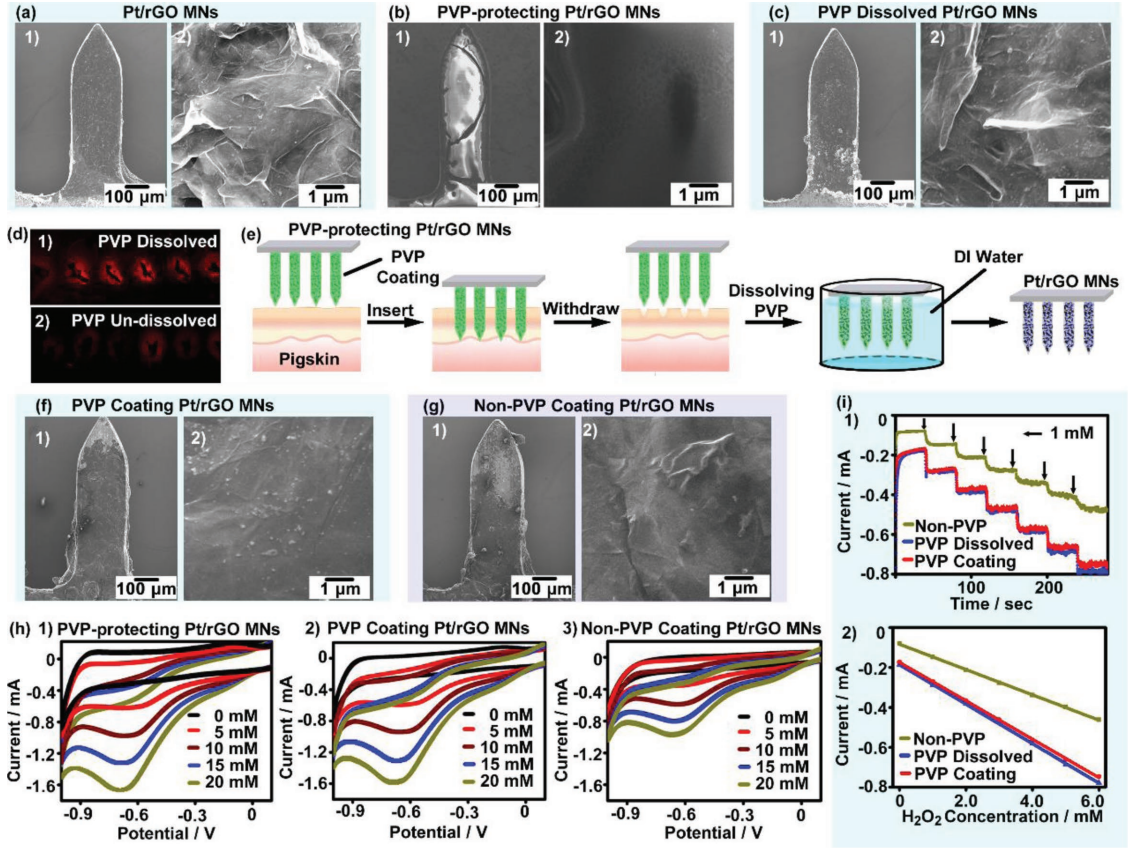

Figure 4. a) SEM images of Pt/rGO MNs without PVP coating at different zoom-in magnifications. b) SEM images of Pt/rGO MNs coated with PVP layer. c) SEM images of the recovered surface morphology of Pt/rGO MNs. PVP layer was coated on the MNs and then dissolved in DI water to re-expose the MN surface. d1) Fluorescence images showing deposition of Rhodamine B (red fluorescence) in the skin by MN-mediated delivery. MNs were coated with PVP layer prestained with Rhodamine B. d2) While the MNs were pressed on skin shortly for only 5 s, the PVP has not been dissolved to release Rhodamine B in skin. e) Illustration of the experiment investigating whether the PVP coating protected Pt/rGO when MNs were inserted into skin. The PVP-protecting Pt/rGO MNs were inserted into skin shortly and withdrawn, then the PVP was dissolved in water. f) SEM images of the PVP Coating and g) Non-PVP Coating Pt/rGO MNs after pigskin insertion. h) CV results of PVP-protecting Pt/rGO MNs (without skin insertion), PVP Coating and Non-PVP Coating MNs (both inserted into skin for 5 s and then withdrawn). i) The amperometric responses of MNs upon the subsequent addition of H_2O_2 in PBS at –0.7 V. The H_2O_2 concentration was stepwise increased by 1×10^{-3} M every 40 s (black arrows). The relations of the steady-state currents and the corresponding H_2O_2 concentration were shown. The data were linearly fitted.

sensing performance, yet these nanostructures could be easily destructed when MNs were inserted into skin due to mechanical frictions. To avoid this, water-dissolvable and biocompatible polymer, polyvinylpyrrolidone (PVP), was spay-coated on the Pt/rGO MN as protecting layer. After PVP coating, the MNs were imaged with SEM to examine the surface. The results revealed that the MN surface was uniformly and conformally covered by a polymer layer with the thickness of ≈2 μm (Figure 4b). The nanostructural Pt/rGO were fully embedded within the polymer layer. When the MNs were immersed in DI water for 5 min to dissolve the PVP coating (Section S6.1, Supporting Information), the Pt/rGO nanostructures could be exposed on the MN surface again (Figure 4c). To examine whether Pt/rGO MNs could effectively penetrate into skin tissue, the PVP layer was prestained with red fluorescent dye, Rhodamine B, and then spay-coated on MNs. The MNs were pressed against a piece of pigskin for 5 min and then withdrawn. Red fluorescence was observed around the penetration sites in the skin (Section S6.2, Supporting Information), indicating that the PVP was dissolved and the red fluorescent dye was released and deposited in the skin (Figure 4d1). While the MNs were pressed against the pigskin shortly for 5 s only and then withdrawn, no fluorescence was detected in the skin (Figure 4d2), suggesting that the PVP was not dissolved in the epidermis to release the fluorescent dye during such a short exposure time. Indeed, the PVP coating on this immediately withdrawn MNs was found to be intact via SEM (Section S6.3, Supporting Information), consistent with the fluorescence results.

To investigate whether the PVP coating could effectively prevent destruction of Pt/rGO nanostructures when MNs were inserted into skin, the MN surface morphology after penetrating pigskin was examined (Section S6.4, Supporting Information). In this experiment (Figure 4e), the PVP-protecting Pt/rGO MNs were pressed against pigskin shortly for 5 s, rather than 5 min, and then immediately withdrawn from the skin. The MN tips were immersed in the epidermis for only 5 s, and the PVP had not been dissolved in the epidermis during such a short exposure time. Therefore, the remaining PVP coating could prevent Pt/rGO destruction when the MNs were withdrawn from skin for SEM imaging. The MNs were then immersed in DI water to further dissolve the PVP coating to reveal the surface. The results found that the Pt/rGO on MN surface remained relatively intact after this insertion/withdrawing process (Figure 4f). By contrast, when Pt/rGO MNs without PVP coating were inserted into skin shortly for 5 s and withdrawn immediately, parts of the Pt/rGO on MN surface were found to be destructed or peeled off (Figure 4g). These results suggested that the PVP coating could effectively protect nanostructural Pt/rGO on MN surface from mechanical destructions during the process of MN penetrating skin, which is a tough issue that has hindered the development of hierarchical MNs incorporating surficial nanostructures.

The electrochemical sensing performance of the Pt/rGO MNs after skin penetration was further evaluated. PVP-protecting Pt/rGO MNs were immersed in DI water to dissolve the PVP coating (denoted as "PVP Dissolved"), and then applied as working electrode to sense H_2O_2 solution via CV. The CV results of sensing H_2O_2 at the concentration of 0, 5×10^{-3}, 10×10^{-3}, 15×10^{-3}, and 20×10^{-3} M H_2O_2 in the PBS solution were shown in Figure 4h1. Significant oxidative and reductive peaks in the potential range of –1.0 to 0.1 V were observed, in a similar profile as the Pt/rGO MNs without PVP-coating and dissolving treatment (Figure 3d). In another experiment, the PVP-protecting Pt/rGO MNs were pressed against pigskin for 5 s and then immediately withdrawn, and immersed into DI water to further dissolve the PVP coating, as illustrated in Figure 4e. The revealed MNs (denoted as "PVP Coating," Section S7.1, Supporting Information) were then applied as working electrode to sense H_2O_2 solution via CV. Similarly, significant oxidative and reductive peaks in the potential range of –1.0 to 0.1 V were observed as well (Figure 4h2), and the CV results did not significantly differ from the results on the Pt/rGO MNs without skin-penetration treatments (Figure 4h1). By contrast, if the Pt/rGO MNs were unprotected by PVP coating (denoted as "Non-PVP Coating"), after skin penetration, the MNs showed significantly compromised CV peak signals (Figure 4h3).

The amperometric response of the above MN electrodes, the PVP Dissolved, PVP Coating, and Non-PVP Coating, were tested (Figure 4i). The MN electrodes were placed in the H_2O_2 solution, and then H_2O_2 concentrations were increased from 0 to 6×10^{-3} M by 1×10^{-3} M every 40 s in a stepwise manner. The time points when H_2O_2 was increased were indicated with black arrows in Figure 4i1. The electrical current was recorded at the applied potential of –0.7 V at the scanning rate of 50 mV s^{-1}. The subsequent addition of 1×10^{-3} M H_2O_2 to the PVP Dissolved, PVP Coating could also induce detectable electrical signals of ≈0.12 mA. The relation of the steady-state current and the corresponding H_2O_2 concentration was shown in Figure 4i2 and Section S7.2 (Supporting Information). These results indicate that PVP coating could successfully avoid destruction of Pt/rGO nanostructures when MNs were inserted into skin and facilitate the Pt/rGO MN process outstanding electrochemical sensing performance after skin penetration.

To demonstrate in situ and real-time H_2O_2 sensing in actual biological tissue, the Pt/rGO MNs were employed to detect H_2O_2 in pigskin. The sensor was based on three-electrode system, where three individual MN patches were applied (**Figure 5**a). The Pt/rGO MN patch was used as the working electrode (W.E), and was precoated with PVP for protection; metal MN patch sputter-coated with Pt was used as the counter electrode (C.E); metal MN patch was dip-coated with Ag/AgCl as the reference electrode (R.E). The MN electrode patches were separated by nonconductive plastic resin, and the three MN patches were integrated as a whole sensor (Sections S8.1 and S8.2, Supporting Information). The surface morphologies of the Pt MN counter electrode and Ag/AgCl reference electrode were imaged with SEM, and were found to be relatively smooth similar as the blank MNs (Figure 5b). Pieces of pigskin with similar sizes were soaked in PBS solution containing different concentrations of H_2O_2 (0, 0.5, 1, and 2 M) for 24 h, allowing H_2O_2 diffusion into the skin tissue to saturate. To determine the actual H_2O_2 concentration in the pigskin tissues, the skin tissues were minced and quantitatively measured with H_2O_2 detection kit, and the H_2O_2 concentrations in different tissue samples were determined to be 0, 0.2×10^{-3}, 0.4×10^{-3}, and 0.8×10^{-3} M, respectively

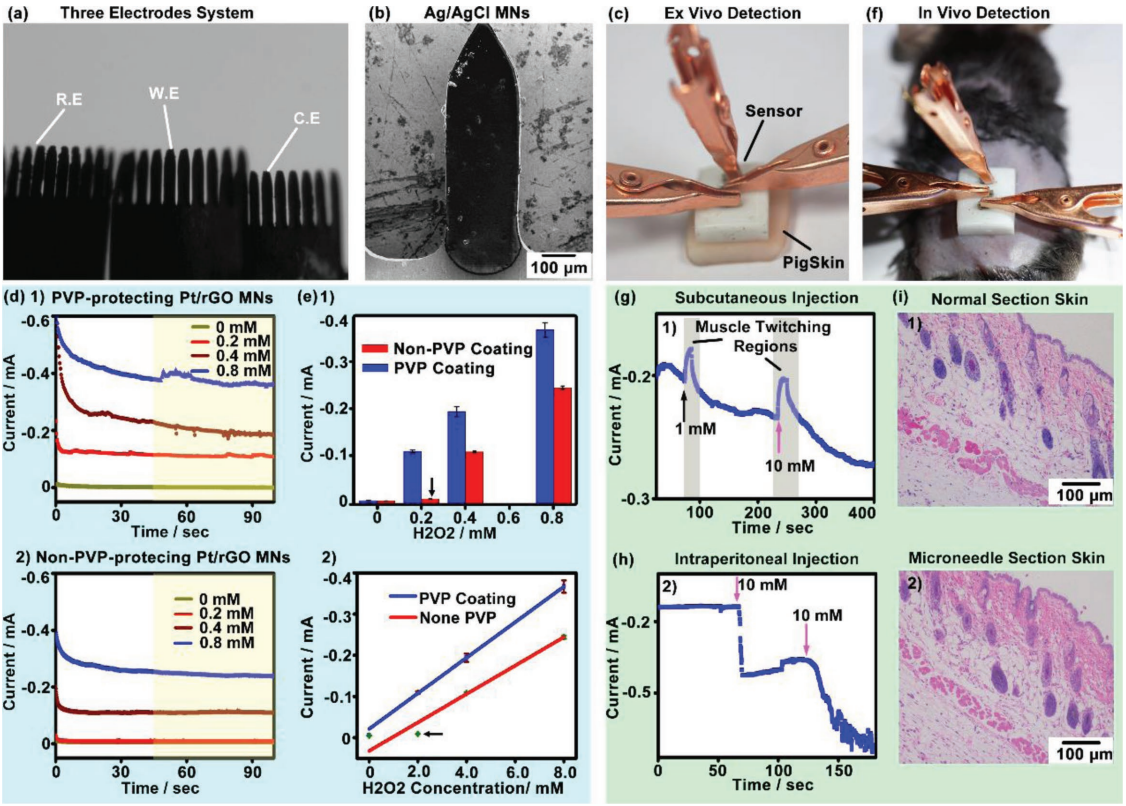

Figure 5. a) Optical microscopic image of three-electrode sensor system including the R.E, W.E, and C.E. b) SEM image of Ag/AgCl MN. c) Photographic image of MN sensor applied on the skin surface for ex vivo H_2O_2 sensing. d) Amperometric responses of MN sensors upon the sensing on pigskin containing H_2O_2 of various concentrations. The regions of stabilized current signals were indicated with yellow color. e) Statistical analysis of the steady-state currents in (d), and the relations of the steady-state currents and the corresponding H_2O_2 concentration. The data were linearly fitted. Black arrows indicated the failure of detection of H_2O_2 concentration lower than 0.2×10^{-3} M. f) Photographic image of MN-based sensor applied on mice to detect H_2O_2 in vivo. g) Amperometric responses of MN sensors upon the sensing on mice. The mice were s.c. injected with 1×10^{-3} and 10×10^{-3} M H_2O_2 solutions at the time points $t = 70$ s and $t = 230$ s (indicated with arrows). The gray region indicated the period of sudden mice muscle twitch caused by metal needle injection. h) Amperometric responses of MN sensors upon the sensing on mice. The mice were i.p. injected with 10×10^{-3} M H_2O_2 solutions at the time points $t = 70$ s and $t = 130$ s (indicated with arrows). i) Optical microscopic images of skin irritation assay. MN-treated local skin tissue was stained with hematoxylin and eosin (H&E).

(Section S9.1, Supporting Information). The sensors based on PVP-protecting Pt/rGO MNs were applied on the skin surface (Figure 5c). After waiting for 5 min for the PVP to completely dissolve, the H_2O_2 signals were recorded at the applied potential of –0.7 V (Figure 5d1). The current signals stabilized to reach steady state in 45 s after recording started (yellow regions in Figure 5d). The steady-state signals increased with the increasing of tissue H_2O_2 concentrations. To demonstrate the importance of the PVP protection, sensors based on Pt/rGO MNs without PVP coating were applied on the pigskin (Figure 5d2). The results found that the sensor without PVP coating was able to record signals for tissue with H_2O_2 concentration higher than 0.4×10^{-3} M, but with lower signal amplitudes compared to the PVP-protecting Pt/rGO MNs sensor (Figure 5e and Section S9.2 (Supporting Information)). The non-PVP-protecting sensor failed to detect H_2O_2 when then tissue contained H_2O_2 concentration lower than 0.2×10^{-3} M (indicated with black arrow in Figure 5e), indicating the comprised sensitivity due to the disruption of Pt/rGO nanostructures after skin penetration. These results demonstrated that the sensor based on MNs functionalized with nanostructural Pt/rGO could stably detect H_2O_2 in biological tissue with reasonable sensitivity, and the PVP coating effectively preserve the MN sensing performance to be free of mechanical destructions after by skin insertion process.

To further demonstrate in situ and real-time H_2O_2 sensing in live animal, the PVP-protecting Pt/rGO MN–based sensor was employed on C57BL/6 mice to detect H_2O_2 in vivo (Figure 5f). The mice were anesthetized, then the hair on the back was shaved. Prior to recording, the sensors integrated with MN patch electrodes were pressed against the mouse's back. After waiting for 5 min to allow PVP-protecting layer to completely dissolve, the electrical signals were recorded at the potential of –0.7 V (Figure 5g). To induce fluctuation of H_2O_2 levels in vivo, the mice were subcutaneously (s.c.) injected with 0.3 mL PBS solution containing 1×10^{-3} M H_2O_2 at the time point $t = 70$ s (indicated with black arrow in Figure 5g). The electrical current immediately decreased for an extremely short period (<20 s, indicated with gray band), which was due to the sudden muscle twitch of mice caused by metal needle injection. The electrical signal then gradually increased, likely due to the gradual diffusion of H_2O_2 from the injection site to the local tissue near the MNs. At the time

point $t = 230$ s (indicated with pink arrow), the mice were s.c. injected again with 0.3 mL PBS solution containing 10×10^{-3} M H_2O_2. Followed by a rapid decrease of electrical current (indicated with gray band) due to the sudden muscle twitch of mice, the electrical signal gradually increased again.

In a separated experiment, a C57BL/6 mouse was treated with Pt/rGO MN–based sensor using similar procedure, but the fluctuation of in vivo H_2O_2 level was induced by intraperitoneal (i.p.) injection with 0.3 mL PBS solution containing 10×10^{-3} M H_2O_2. After i.p. injection at the time point $t = 70$ s (indicated with pink arrow in Figure 5h), the electrical signal did not show rapid fluctuation due to muscle twitch in mice this time, but showed an immediate (within 5 s) increase of electrical signal by 0.3 mA. The electrical signal was a steady state within 30 s after i.p. injection, indicating the rapid diffusion of H_2O_2 from the intraperitoneal space to the local tissue near MNs. At the time point $t = 130$ s (pink arrow), i.p. injection was performed again with 0.3 mL PBS solution containing 10×10^{-3} M H_2O_2. Similar to the result of the i.p. injection of the first time, the electrical current increased by 0.3 mA within 5 s, followed by current saturation after 30 s. These results demonstrated that the PVP-protecting Pt/rGO MN–based sensor could successfully and sensitively detect H_2O_2 levels in vivo.

The biocompatibility and biosafety of the PVP-protecting Pt/rGO MN–based sensor were evaluated by histological examination of the induced skin irritation and inflammatory effects after MN penetrations. The MN-based sensor was pressed against the back of mice for 10 min. The MN sensors were removed, and the mice were returned to cage. After 12 h, the MN-treated local skin tissue was dissected, fixed, and then stained with hematoxylin and eosin (H&E). Using normal skin tissue without MN treatment as control group for comparison (Figure 5i1), the MN-treated tissue did not show obvious infiltrated inflammatory cells (Figure 5i2), indicating no significant skin irritation and inflammation were induced after the application of the Pt/rGO MN–based sensor (Section S10, Supporting Information).

2. Conclusion

In this work, conductive MN patch was integrated with nanostructural hybrid materials, the Pt/rGO, as sensitive and mini-invasive transdermal electrode for H_2O_2 sensing. The Pt/rGO present on MN surface acted as the electrochemical sensing modulus, which significantly improved the detection sensitivity of the MN electrode. The MNs were employed as transdermal tool for carrying the Pt/rGO sensing modulus to access the in vivo environment, in a painless and mini-invasive manner. To avoid potential mechanical friction during the process of MN inserting skin, the Pt/rGO nanostructures were protected by a water-soluble polymer layer. The sensing capability and sensitivity of the Pt/rGO MNs were well preserved by the polymer coating protection. The applications of the Pt/rGO MNs for in situ and real-time detection of H_2O_2 in vivo were demonstrated both on pigskin and living mice. This work provided a unique real-time and in vivo biosensing system that takes advantages of the high sensitivity of hybrid nanomaterials and the mini-invasive nature of MN patch. By specifically functioning the nanostructural sensing modulus, this system would be readily extended to sensing a wide range of biomarkers for rapid and continuous disease monitoring.

3. Experimental Section

Steel MN Patch Fabrication: The steel MN patch was fabricated by laser microetching (INNO LASER) on a stainless steel substrate (thickness ≈ 100 µm, Kveiner). Each steel MN patch contained 10 MNs; the MN length was 800 µm; the MN width was 225 µm; the inter-MN space of MN was 250 µm.

Preparation of GO/H_2PtCl_6 Coating on MN Surface: Before coating process, the steel MN patch was placed in ethanol solution and sonicated for 5 min to remove impurities on the surface of MNs and sterilize MN patch. The MN was then treated with O_2 plasma (Dynetech, PT-5SM) for 5 min (at the power of 75 W) to increase the hydrophilicity of the MN surface, in order to facilitate absorption of the coating layer. The pretreated MN patch was immersed in the 10 mL 0.05 % H_2PtCl_6 (Sigma-Aldrich) aqueous solution containing 0.1 g GO (Suzhou Carbon Technology Co., Ltd.). Dip-coating process was repeated for 3 times, allowing GO to layer-by-layer assemble on the MN surface. The MN patch was then dried at room temperature to obtain uniform GO/H_2PtCl_6 coated on the metal MN patch.

Preparation of Pt/rGO Coating on MN Surface: The above prepared GO/H_2PtCl_6 MN patch was placed in 10 mL aqueous solution of 10% vitamin C (Sigma-Aldrich) at 95 °C for 3 h to carry out the chemical reduction process, which turned the GO/H_2PtCl_6 into Pt/rGO. After reduction process, Pt/rGO MN patch was washed with DI water for 3 times to remove impurities from the MN surface.

Preparation of rGO Coating on MN Surface: For a comparison with the Pt/rGO-coated MN, a MN with only rGO coating was also fabricated. Followed with the same pretreatment (cleaning and plasma treatment) processing, the MN was immersed in the 10 mL aqueous solution only containing 0.1 g GO, repeating 3 times to guarantee the layer-by-layer assembling of GO on the MN surface. The MN patch was then dried at room temperature to obtain uniform GO coated on the metal MN patch. Then, the prepared GO/MN patch was placed in 10 mL 10 wt% vitamin C solution at 95 °C for 3 h, turning the GO into rGO. Afterward, rGO MN patch was rinsed in DI water for 3 times to remove impurities.

Preparation of Ag/AgCl and Pt Coating on MN Surface: Ag/AgCl MNs as reference electrode were prepared by dip-coating process to absorb Ag/AgCl coated on the MN surface. Blank steel MN patch was immersed in Ag/AgCl conductive inks (ALS Co., Ltd.) to allow Ag/AgCl to deposit on the MN surface. To fabricate Pt MNs as counter electrode, blank MN was treated with O_2 plasma for 5 min and then magnetron sputtering(VTC-600-3HD, Zhongke Desheng Technology Co., Ltd.) was used to sputter Ti/Pt thin layer (≈20/20 nm) on the MN surface.

Preparation of PVP Protecting Layer on the Pt/rGO MN: PVP (Molecular Weight ≈ 55k, Sigma-Aldrich) was used as the protecting layer coating on the MN surface, because it could be coated as a thin layer covering the MN surface and could also be rapidly dissolved in aqueous solution. Ethanol solution containing 10% PVP was uniformly deposited on the MN surface by spray coating and then dried at room temperature.

Preparation of MN Three-Electrode Sensor: In order to ensure the MN sensing device to work stably during the detection process, the three MN electrode patches were encapsulated in a plastic resin mold prepared via 3D printing (Formlabs, Form 2). The length, width, and thickness of the mold were 12, 10, and 1.2 mm, respectively. There were three channels in the center of the mold to fix the three electrodes, where the MN bases could be encapsulated by the mold, while the MN tips were exposed as the electrochemical sensing part. The distance between MN electrode in the mold was around 1 mm. The fixed MNs were further encapsulated by poly-di-methyl siloxane (PDMS, Sylgard 184, Dow Corning, MI), so that a tight insulating layer was formed around the MN electrode.

Characterization of MN Arrays: The surface morphology of MN patches was characterized by scanning electron microscopy (SEM, SUPRA 60, Zeiss) or optical microscope (Axio Scope A1, Zeiss). The contact angle

measurements of surface were performed using goniometer measuring system (Kurss, DSA 15). DI water droplets of 3 µL were tested as probe liquids. The surface element analysis was performed using EDX (Oxford Instrument).

Fluorescence Microscopy Examination of MN Penetration into Skin: The PVP in ethanol solution was premixed with red fluorescent dye, Rhodamine B, and then spay-coated on MNs. The MNs were pressed against pigskin for either 5 s or 5 min and then withdrawn. The tissue was then imaged with fluorescence microscopy to examine whether fluorescence dye deposited around the penetration sites in the skin.

Examination of Surface Morphology of MNs after Skin Penetration: The PVP-protecting Pt/rGO MNs were pressed against pigskin shortly for 5 s, rather than 5 min, and then immediately withdrawn from the skin. The MN tips were immersed in the epidermis for only 5 s, and the PVP was not dissolved in the epidermis during such a short exposure time. Therefore, the remaining PVP coating could prevent Pt/rGO destruction when the MNs were withdrawn from skin for SEM imaging. The MNs were then immersed in DI water to further dissolve the PVP coating to reveal the surface. More specifically, Pt/rGO MNs coated with PVP were inserted into pigskin shortly for 5 s and then immediately withdrawn. The MNs were then immersed into DI water to further dissolve the PVP coating. This MN patch was denoted as "PVP Coating." By contrast, if the Pt/rGO MNs were not precoated with PVP, the MN patch was denoted as "Non-PVP Coating." If PVP-protecting Pt/rGO MNs were immersed in DI water to dissolve the PVP coating, but without penetrating skin, this MN patch was named "PVP Dissolved."

Electrochemical Sensing In Vitro: A standard three-electrode electrochemical workstation (CH Instrument, 700E) at room temperature was used to examine the electrochemical property of the samples. The MN patch as working electrode was coupled with a commercial Ag/AgCl reference electrode and a commercial Pt counter electrode. The electrochemical activities of the MNs were evaluated via CV. The CV results of sensing H_2O_2 at the concentration of 0, 5×10^{-3}, 10×10^{-3}, 15×10^{-3}, and 20×10^{-3} M in PBS solution (pH 7.0) were performed at the scanning potential range of –1.0 to 0.1 V. For the testing of amperometric response upon H_2O_2 additions, the sensing was tested at the applied potential of –0.7 V. The H_2O_2 concentration was stepwise increased by 1×10^{-3} M every 40 s, from 0 to 6×10^{-3} M. Alternatively, to examine the sensing of H_2O_2 concentration, H_2O_2 concentration was stepwise increased by 0.1×10^{-3} M every 50 s up to 0.5×10^{-3} M, and then stepwise increased by 0.5×10^{-3} M every 50 s up to 3×10^{-3} M, and finally stepwise increased by 1×10^{-3} M every 50 s up to 8×10^{-3} M.

Application of Three-Electrode MN Sensor Ex Vivo on Pigskin Model: Prior to the MN insertion, 75% alcohol was used to washed and disinfected pigskins (1.5 cm × 1.5 cm × 3 mm). The pigskin was immersed and soaked in PBS solution containing different concentrations of H_2O_2 (0, 0.5, 1, and 2 M) for 24 h, allowing H_2O_2 diffusion into the skin tissue to saturate. PVP-protecting Pt/rGO MNs patch was pressed against the pigskin and the electrical current signals were recorded at the applied potential range of –0.7 V. To determine the actual H_2O_2 concentration in the pigskin tissues, the skin tissues were minced and quantitatively measured with H_2O_2 detection kit (Beyotime Biotechnology), so that the H_2O_2 concentrations in different tissue samples were quantified.

Application of Three-Electrode MN Sensor In Vivo on Mice Model: Animal studies were approved by the Sun Yat-sen University Institutional Animal Care and Use Committee. All animals received humane care in compliance with institutional guidelines. C57BL/6 mice were obtained from the Animal Facility of Sun Yat-Sen University. Animal studies were performed at the Animal Facility of Sun Yat-Sen University. The mice were anesthetized and the hair on the mice's dorsum was removed without wound the skin. The MN sensor was pressed against the mice's back. After waiting for 5 min to allow PVP-protecting layer to completely dissolve, the electrical signals were recorded at the potential of –0.7 V. For the H_2O_2 fluctuation induced by subcutaneous injection, at the indicated time points, the mice were s.c. injected with 0.3 mL PBS solution containing 1×10^{-3} M or 10×10^{-3} M H_2O_2. For the H_2O_2 fluctuation induced by i.p. injection, the mice were i.p. injected with 0.3 mL PBS solution containing 10×10^{-3} M H_2O_2 at the indicated time points.

H_2O_2 Detection Procedures In Vivo Using Living Mice: Animal experiments of living mice were carried out under anesthesia. Prior to the H_2O_2 detection procedures, all mice were anesthetized by an intraperitoneal injection of 3% sodium pentobarbital solution (1.0–1.5 mL kg^{-1}; Merck, USA). During H_2O_2 detection procedure, the anesthetized mice were placed on an animal thermostatic surgical blanket to maintain their body temperature and in a natural prone position. During the whole test, the mice did not had any big physical movements, only had regular movements of breathing.

Biocompatibility and Biosafety Tests of MN Applications: Local skin irritation caused by sensor application was tested. The MN sensor was pressed against the back of mice for 10 min. The MN sensor were removed, and the mice were returned to cage. After 12 h, the MN-treated local skin tissue was dissected, fixed, and then stained with H&E. The tissue profile was examined with optical microscopy (M-shot).

Supporting Information

Supporting Information is available from the Wiley Online Library or from the author.

Acknowledgements

Q.J. and H.-J.C. contributed equally to this work. This work was supported in part by the National Natural Science Foundation of China (Grant Nos. 61771498, 51705543, and 31530023). The authors wish to thank the Youth 1000 Talents Program of China and the 100 Talents Program of Sun Yat-Sen University and the Youth Teacher Training Program of Sun Yat-Sen University (Grant Nos. 76120-18821104, 18lgpy18, 18lgpy21), the Science and Technology Program of Guangzhou, China (Grant No. 201803010097), and the Science and Technology Planning Project of Guangdong Province for Industrial Applications (Grant No. 2017B090917001).

Conflict of Interest

The authors declare no conflict of interest.

Keywords

microneedle sensors, mini-invasive and painless, nanohybrid electrodes, real-time biosensors, transdermal electrodes

Received: October 15, 2018
Revised: December 14, 2018
Published online:

[1] R. K. Mishra, A. M. Vinu Mohan, F. Soto, R. Chrostowski, J. Wang, *Analyst* **2017**, *142*, 918.
[2] J. L. Hammond, N. Formisano, P. Estrela, S. Carrara, J. Tkac, *Essays Biochem.* **2016**, *60*, 69.
[3] H. A. Abdulbari, E. A. M. Basheer, *ChemBioEng Rev.* **2017**, *4*, 92.
[4] Y. Zhang, C. Wu, X. Zhou, X. Wu, Y. Yang, H. Wu, S. Guo, J. Zhang, *Nanoscale* **2013**, *5*, 1816.
[5] Y. Zhang, X. Bai, X. Wang, K. K. Shiu, Y. Zhu, H. Jiang, *Anal. Chem.* **2014**, *86*, 9459.
[6] T. Wang, H. Zhu, J. Zhuo, Z. Zhu, P. Papakonstantinou, G. Lubarsky, J. Lin, M. Li, *Anal. Chem.* **2013**, *85*, 10289.
[7] F. Xie, X. Cao, F. Qu, A. M. Asiri, X. Sun, *Sens. Actuators, B* **2018**, *255*, 1254.

[8] S. Varma, P. Devamanoharan, *Free Radical Res. Commun.* **1991**, *14*, 125.
[9] B. Halliwell, M. V. Clement, L. H. Long, *FEBS Lett.* **2000**, *486*, 10.
[10] M. Giorgio, M. Trinei, E. Migliaccio, P. G. Pelicci, *Nat. Rev. Mol. Cell Biol.* **2007**, *8*, 722.
[11] M.-V. Clément, S. Pervaiz, *Redox Rep.* **2001**, *6*, 211.
[12] X. Sun, S. Guo, Y. Liu, S. Sun, *Nano Lett.* **2012**, *12*, 4859.
[13] Y. Fu, D. Huang, C. Li, L. Zou, B. Ye, *Anal. Chim. Acta* **2018**, *1014*, 10.
[14] G. Miller, K. Schlauch, R. Tam, D. Cortes, M. A. Torres, V. Shulaev, J. L. Dangl, R. Mittler, *Sci. Signaling* **2009**, *2*, ra45.
[15] L. Ventrelli, L. Marsilio Strambini, G. Barillaro, *Adv. Healthcare Mater.* **2015**, *4*, 2606.
[16] X. Zhao, W. Gao, W. Yao, Y. Jiang, Z. Xu, C. Gao, *ACS Nano* **2017**, *11*, 9663.
[17] L. Dong, R. R. S. Gari, Z. Li, M. M. Craig, S. Hou, *Carbon* **2010**, *48*, 781.
[18] J. Bai, X. Jiang, *Anal. Chem.* **2013**, *85*, 8095.
[19] J. Wei, Z. Zang, Y. Zhang, M. Wang, J. Du, X. Tang, *Opt. Lett.* **2017**, *42*, 911.
[20] S. Pourhashem, M. R. Vaezi, A. Rashidi, M. R. Bagherzadeh, *Corros. Sci.* **2017**, *115*, 78.
[21] L. Strambini, A. Longo, S. Scarano, T. Prescimone, I. Palchetti, M. Minunni, D. Giannessi, G. Barillaro, *Biosens. Bioelectron.* **2015**, *66*, 162.
[22] T.-Q. Xu, Q.-L. Zhang, J.-N. Zheng, Z.-Y. Lv, J. Wei, A.-J. Wang, J.-J. Feng, *Electrochim. Acta* **2014**, *115*, 109.
[23] C. L. Sun, H. H. Lee, J. M. Yang, C. C. Wu, *Biosens. Bioelectron.* **2011**, *26*, 3450.
[24] A. T. Lawal, *Talanta* **2015**, *131*, 424.
[25] Z. Li, C. Xie, J. Wang, A. Meng, F. Zhang, *Sens. Actuators, B* **2015**, *208*, 505.
[26] Y. Li, W. Gao, L. Ci, C. Wang, P. M. Ajayan, *Carbon* **2010**, *48*, 1124.
[27] Y. Li, L. Tang, J. Li, *Electrochem. Commun.* **2009**, *11*, 846.
[28] P. R. Miller, S. D. Gittard, T. L. Edwards, D. M. Lopez, X. Xiao, D. R. Wheeler, N. A. Monteiro-Riviere, S. M. Brozik, R. Polsky, R. J. Narayan, *Biomicrofluidics* **2011**, *5*, 013415.
[29] S. A. Ranamukhaarachchi, C. Padeste, M. Dubner, U. O. Hafeli, B. Stoeber, V. J. Cadarso, *Sci. Rep.* **2016**, *6*, 29075.
[30] P. Bollella, S. Sharma, A. E. G. Cass, R. Antiochia, *Biosens. Bioelectron.* **2019**, *123*, 152.
[31] S. R. Chinnadayyala, I. Park, S. Cho, *Microchim. Acta* **2018**, *185*, 250.
[32] S. J. Lee, H. S. Yoon, X. Xuan, J. Y. Park, S.-J. Paik, M. G. Allen, *Sens. Actuators, B* **2016**, *222*, 1144.
[33] J. Yang, Z. Chen, R. Ye, J. Li, Y. Lin, J. Gao, L. Ren, B. Liu, L. Jiang, *Drug Delivery* **2018**, *25*, 1728.
[34] G. Traverso, C. M. Schoellhammer, A. Schroeder, R. Maa, G. Y. Lauwers, B. E. Polat, D. G. Anderson, D. Blankschtein, R. Langer, *J. Pharm. Sci.* **2015**, *104*, 362.
[35] M. R. Prausnitz, *Annu. Rev. Chem. Biomol. Eng.* **2017**, *8*, 177.
[36] H. Lee, C. Song, Y. S. Hong, S. K. Min, H. R. Cho, T. Kang, K. Shin, S. H. Choi, T. Hyeon, D. H. Kim, *Sci. Adv.* **2017**, *3*, e1601314.
[37] R. F. Donnelly, M. T. Mccrudden, A. A. Zaid, E. Larrañeta, E. Mcalister, A. J. Courtenay, M. C. Kearney, T. R. Singh, H. O. Mccarthy, V. L. Kett, *PLoS One* **2014**, *9*, e111547.
[38] X. Xie, C. Pascual, C. Lieu, S. Oh, J. Wang, B. Zou, J. Xie, Z. Li, J. Xie, D. C. Yeomans, M. X. Wu, X. S. Xie, *ACS Nano* **2017**, *11*, 395.
[39] K. Y. Hwa, B. Subramani, P. W. Chang, M. Chien, J. T. Huang, *Int. J. Electrochem. Sci.* **2015**, *10*, 2455.
[40] S. Sharma, A. Saeed, C. Johnson, N. Gadegaard, A. E. Cass, *Sens. Bio-Sens. Res.* **2017**, *13*, 104.
[41] Y. Li, W. Gao, L. Ci, W. Wang, P. M. Ajayan, *Carbon* **2010**, *48*, 1124.
[42] G. G. Kumar, C. J. Kirubaharan, S. Udhayakumar, C. Karthikeyan, K. S. Nahm, *Ind. Eng. Chem. Res.* **2014**, *53*, 16883.
[43] C. Chen, M. Long, H. Wu, W. Cai, *Sci. China Chem.* **2013**, *56*, 354.